Journal of Advanced Research 22 (2020) 85–97

Contents lists available at ScienceDirect

Journal of Advanced Research

journal homepage: www.elsevier.com/locate/jare

Structure and electrochemical properties of carbon nanostructures derived from nickel(II) and iron(II) phthalocyanines

Angela Sanchez-Sanchez [a,*], Maria Teresa Izquierdo [b], Sandrine Mathieu [c], Jaafar Ghanbaja [c], Alain Celzard [a,*], Vanessa Fierro [a]

[a] Université de Lorraine, CNRS, IJL, F-88000 Epinal, France
[b] Instituto de Carboquimica, ICB-CSIC, Miguel Luesma Castan, 4, 50018 Zaragoza, Spain
[c] Université de Lorraine, CNRS, IJL, F-54000 Nancy, France

GRAPHICAL ABSTRACT

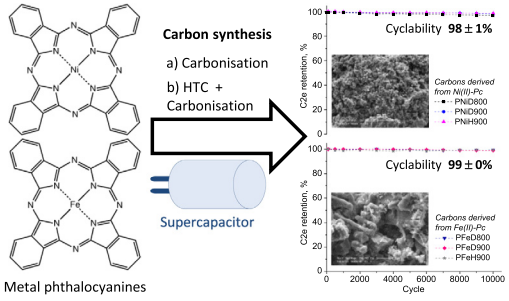

ARTICLE INFO

Article history:
Received 3 September 2019
Revised 28 October 2019
Accepted 10 November 2019
Available online 14 November 2019

Keywords:
Metal phthalocyanines
Hydrothermal carbonisation
Catalytic graphitisation
Supercapacitors

ABSTRACT

Mesoporous carbons containing up to 3.6 at.% N and 4.4 at.% O and exhibiting graphitic character have been prepared from Ni(II) and Fe(II) phthalocyanines by direct pyrolysis or by HTC + pyrolysis, and subsequently applied as supercapacitor materials. No mesoporous templates or doping post-treatments were used, and the catalytic effect of Ni(II) and Fe(II), naturally present in the precursor molecules, allowed obtaining graphitic carbons at temperatures $\leq$ 900 °C. Metals were encapsulated in the core of onion–like structures with no contact with the electrolyte, so that electrodes were prevented from degradation during device operation. The materials exhibited high rate capabilities up to 1 V s^{-1}, higher interfacial capacitances than a wide variety of materials possessing higher surface areas, and high capacitance retentions up to 99% at 5 A g^{-1} current density throughout 10 000 charge–discharge cycles. The electrochemical performances of the phthalocyanine-derived carbons are due to their graphitic character and to the pseudocapacitance contribution of the surface groups through Faradaic reactions. This work opens a new way to obtain carbon materials from a great family of metal phthalocyanines, since the central metal and the radicals of the latter can be varied to tune the carbon properties for specific applications.

Introduction

Metal phthalocyanines are macrocyclic, planar and aromatic complexes of tetrabenzoporphyrazin nature. Most metals have already been introduced at the centre of phthalocyanine macrocycles by slightly changing the synthetic procedure. Depending on

Peer review under responsibility of Cairo University.
* Corresponding authors.
E-mail addresses: angela.sanchez-sanchez@univ-lorraine.fr (A. Sanchez-Sanchez), alain.celzard@univ-lorraine.fr (A. Celzard).

https://doi.org/10.1016/j.jare.2019.11.004
2090-1232/

the central metal, reactivity, electronic and magnetic properties, as well as biological functionality of the resultant complexe may change significantly [1,2]. From their discovery in 1928, metal phthalocyanines have been widely used as commercial dyes and pigments, and more recently as electrocatalysts for fuel cells [3], as models for coal char combustion and pyrolysis [4], as precursors for producing carbon nanotubes [5,6], as photosensitisers for photodynamic therapy [7], as electrode materials for energy storage [8,9], or as components in solar photovoltaic cells [10].

Lately, the use of phthalocyanines to store energy in supercapacitors has attracted increasing attention due to their pseudocapacitive behaviour. Metal phthalocyanines have been primarily used as additives to increase the capacitance of carbon materials, such as multi-walled carbon nanotubes (MWCNTs). Nanocomposite films based on Ni(II) tetra-aminophthalocyanine (NiTAPc) and MWCNTs were found to yield high specific capacitances in 1 mol L^{-1} H_2SO_4 electrolyte thanks to the nitrogen-containing groups on the phthalocyanine ring [8]. Electro-polymeric nickel tetra-aminophthalocyanine (polyNiTAPc) was also supported on MWCNTs and the resultant composite, MWCNT-polyNiTAPc, exhibited excellent stability up to 1000 cycles of charge-discharge [9]. Nevertheless, little work exists on the use of phthalocyanines as precursors of carbon materials and the application of the latter as capacitor electrodes. Metal phthalocyanines based on either Ni, Fe, Co or Mn were used to prepare CMK-3 – type ordered mesoporous carbons (OMCs) exhibiting high graphitic character by a hard-templating method [11]. One of these materials exhibited considerably higher electrochemical performances in 0.5 mol L^{-1} H_2SO_4 than an amorphous CMK-3 material obtained from sucrose with the same silica template, and also presented higher resistance to oxidation owing to its highly graphitic character. However, preparing the silica template is expensive and its removal by dissolution with either HF or NaOH is necessary for recovering the carbon. The latter procedure further increases the cost of the synthesis, generates toxic products, and is therefore not easily scalable at the industrial level.

Hydrothermal carbonisation (HTC) is an environment–friendly technique usually carried out inside autoclaves at mild temperatures (<250 °C) under self-generated pressure, and using water or other poorly hazardous solvents [12]. Given that the reaction is exothermic, the consumption of thermal energy is very low compared to other methods. HTC is a particularly useful method to convert complex structures that do not suffer any structural disruption below 180 °C, such as cellulose, lignin or lignocellulosic biomasses, and subsequent pyrolysis of the obtained hydrochars gives rise to carbon materials that have been extensively investigated as supercapacitor electrodes [12–14]. Other uses included the production of chemicals like phenolic compounds and aldehydes, which can be subsequently processed by bio–refineries [15,16], and the obtention of metal/carbon catalysts from mixtures of carbohydrates and metal salts followed by pyrolysis, which are suitable for a broad range of applications [17–19].

Given the high chemical stability of metal phthalocyanines, HTC would be an excellent "green" method to increase their reactivity in mild conditions of pressure and temperature, simply using water as solvent. Moreover, the central metal of the phthalocyanine can be selected for catalysing the graphitisation of the resultant carbon material at temperatures lower than those generally required for that purpose, which are typically higher than 2000 °C [20–22]. Catalytic graphitisation using metals such as Fe or Ni therefore saves energy, decreases the synthesis cost, is easy to proceed, and can be applied to carbons considered as non-graphitisable in usual conditions of thermal treatment [23]. Using Fe(II) or Ni(II) phthalocyanines (Fig. 1) as simultaneous carbon precursor and graphitisation catalyst should also ensure an excellent mixing, at the atomic scale, of carbon source and metal catalyst, which strongly influences the extent of the graphitisation process [24].

The aim of the present work was to evaluate the synthesis of N-doped graphitic carbons from Fe(II) and Ni(II) phthalocyanines and investigate their electrochemical properties in terms of energy storage in capacitors. The carbon materials were obtained either by direct pyrolysis of metal phthalocyanines at 800 or 900 °C, or by submitting them first to HTC in water, followed by pyrolysis at 900 °C. The resultant carbons contained nitrogen and oxygen, and exhibited mesoporous textures whereas neither additional doping post-treatment or mesoporous templates were used, and also exhibited high graphitisation degrees, despite their low temperatures of pyrolysis. This work opens a new way to transform a broad range of metal phthalocyanines, their derivatives, as well as other organometallic complexes into graphitic carbon materials.

Experimental section

Materials preparation

Nickel(II) phthalocyanine (90% purity), iron(II) phthalocyanine (85% purity), hydrochloric acid (37% v/v), carbon black powder (<100 nm) and sulphuric acid (98% v/v) were purchased from Sigma – Aldrich. Polytetrafluoroethylene (PTFE) and glass fibre separator were provided by Aldrich and Pall Life Sciences, respectively. All the materials were used as received.

The carbon materials were synthesised from Ni(II) or Fe (II) phthalocyanines through two different procedures:

(i) Hydrothermal carbonisation (HTC) + pyrolysis: Ni(II) or Fe (II) phthalocyanines (2 g) were added to a certain volume of water (16 mL), and the resultant mixture was placed in an autoclave and thermally treated under autogenous pressure (180 °C, 24 h). The solid was recovered by filtration, dried (105 °C, 12 h) and pyrolysed under nitrogen flow (900 °C, 1 h, 80 mL N_2 min^{-1}, 2 °C min^{-1}).
(ii) Direct pyrolysis: Ni(II) or Fe(II) phthalocyanines (1 g) were directly pyrolysed under nitrogen flow (800 or 900 °C, 1 h, 80 mL N_2 min^{-1}, 2 °C min^{-1}).

The obtained carbons were subsequently treated with a 1 mol L^{-1} HCl solution to remove the surface metals, then thoroughly washed with distilled water until neutral pH, and finally dried in a ventilated oven (105 °C, 12 h). The final materials were called PMeST, where Me is the metal (Ni or Fe); S the synthesis method (H for materials obtained through HTC, or D for those directly pyrolysed), and T is the final temperature of pyrolysis (800 or 900 °C).

Materials characterisation

Nitrogen adsorption-desorption isotherms were obtained at −196 °C using a Micromeritics ASAP 2020 automatic system. Carbon dioxide adsorption isotherms were measured at 0 °C with a Micromeritics ASAP 2420 device. The surface areas were calculated by applying two models to the nitrogen adsorption isotherms: (i) the BET method, leading to A_{BET} (m^2 g^{-1}), and (ii) the Quenched Solid Density Functional Theory (QSDFT) [25], leading to S_{QSDFT} (m^2 g^{-1}). The total pore volume, V_{QSDFT} (cm^3 g^{-1}), were calculated from the pore size distributions obtained through the QSDFT model. The micropore volumes were calculated by applying the Dubinin – Radushkevich (DR) equation to the nitrogen isotherms, leading to $V_{\mu\text{-}N2}$ (cm^3 g^{-1}), and to the carbon dioxide isotherms, leading to $V_{\mu\text{-}CO2}$ (cm^3 g^{-1}). The mesopore volumes were calculated as the difference V_{QSDFT} - ($V_{<0.7}$ + $V_{0.7\text{-}2}$).

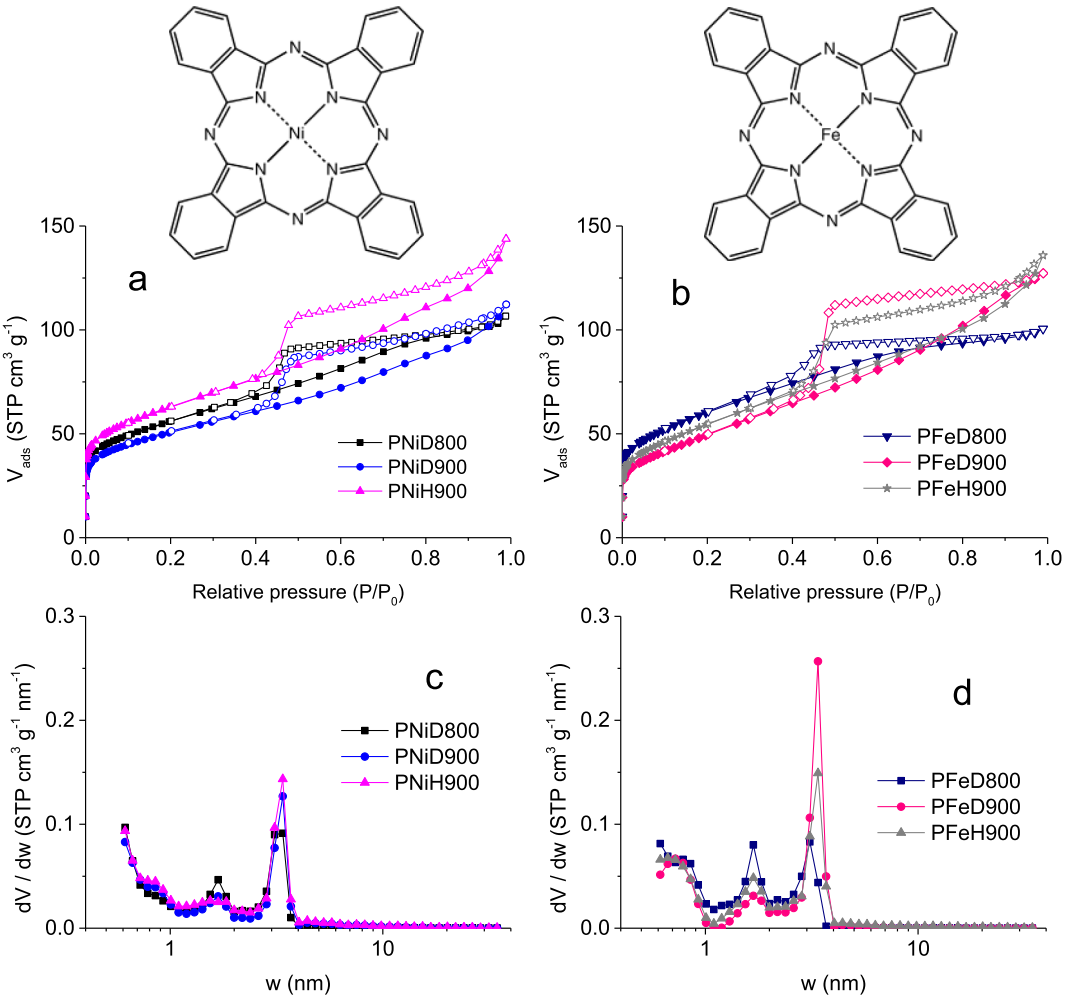

Fig. 1. (a,b) Nitrogen adsorption (full symbols) – desorption (empty symbols) isotherms of the carbon materials; and (c,d) corresponding pore size distributions derived by application of the QSDFT method to the data shown in (a,b). The chemical structure of Ni(II) and Fe(II) phthalocyanines are shown at the top of the figure, on the left and right, respectively. Their molecular formula are $C_{32}H_{16}N_8Ni$ and $C_{32}H_{16}N_8Fe$, respectively, and their molecular weight are 571.23 and 568.36 g mol^{-1}, respectively.

Thermogravimetric analysis (TG) of the HTC-treated phthalocyanines was carried out with a Netzsch STA 449F3 Jupiter microbalance by heating ~20 mg of sample under a flow of either argon or synthetic air (40 mL min^{-1}) up to the final temperature (900 °C, 2 °C min^{-1}).

XRD patterns were collected by a Bruker D8 Advance X-ray powder diffractometer working in Bragg-Brentano configuration and equipped with an X-ray source with a Cu anode working at 40 kV and 40 mA and an energy-dispersive one-dimensional detector. The diffraction patterns were obtained over the 2θ range of 10° to 80° with a step of 0.019°. The assignation of crystalline phases was performed based on Joint Committee on Powder Diffraction Standards. DIFFRAC.EVA software supports a reference pattern database derived from Crystallography Open Database (COD) and the Powder Diffraction File (PDF) for phase identification.

Raman spectroscopy was carried out using a Horiba XploRa Raman spectrometer without sample preparation. The spectra were collected under a microscope using a long-distance 50 × objective. The Raman-scattered light was dispersed by a holographic grating with 1200 lines/mm and detected by a CCD camera. The laser used a wavelength of 532 nm, corresponding to an incident energy of 2.33 eV. The laser was filtered at 1.0% of its nominal power, thus corresponding to 0.14 mW applied to the sample. This value is a compromise between a too high power leading to some visible changes of spectra with time, suggesting heating and damage of the sample under the laser beam, and a too low power for which the signal / noise ratio would have been poor. Each spectrum was obtained by accumulation of two spectra recorded from 800 to 3700 cm^{-1} over 180 s. It was systematically checked that no significant difference was observed when the analysis was performed at different, visually comparable places of the same sample, suggesting the homogeneity of the materials.

Scanning electron microscopy (SEM) images were obtained with a FEI XL30 SFEG electron microscope, and EDX analyses were carried out with an Oxford Instrument (80 mm^2) EDS SDD XMAX detector at 15 kV over an average surface of ~25 × 25 μm. All samples were metallised with carbon to ensure the evacuation of electric charges under the beam. The secondary electron images were taken with an acceleration voltage of 3 or 5 kV to account for the extreme surface of each sample, and an acceleration tension of 10 kV was applied to visualise the distribution of iron and nickel using backscattered electrons.

Transmission electron microscopy (TEM) images were obtained with a Jeol ARM 200F (cold FEG operating at 80 kV) electron microscope.

Elemental analysis was performed with an Elementar Vario EL Cube analyser.

X-ray photoelectron spectroscopy (XPS) spectra were recorded with an ESCAPlus OMICROM system equipped with a hemispherical electron energy analyser. The spectrometer was operated at

10 kV and 15 mA, using a non-monochromatised MgK_{α} X-Ray Source ($h\nu$ = 1253.6 eV) and under vacuum (<5 × 10^{-9} Torr). Analyser pass energies of 50 and 20 eV were used for survey and detailed scans, respectively. Binding energies were referenced to the C1s peak (284.5 eV). A survey scan (1 sweep / 200 ms dwell) was acquired between 1100 and 0 eV. Current region sweeps for Ni2p, Fe2p, O1s, C1s and N1s were obtained. The CASA data processing software allowed smoothing, Shirley-type background subtraction, peak fitting and quantification. Atomic percentages of each element were calculated from intensity ratios using Scofield sensitivity factors [26].

Electrochemical characterisation was performed with a Biologic VMP3 electrochemical workstation. For that purpose, electrodes (10 mg cm^{-2}, 0.5 cm diameter) were prepared from a paste containing the finely pre-ground carbon material, polytetrafluoroethylene (PTFE) binder and carbon black in the weight percent ratio of 85:10:5, and they were afterwards impregnated with the electrolyte (2 mol L^{-1} H_2SO_4, 4 days) under vacuum.

The electrical conductivity of these electrodes was measured by using the four–probe method with a Keithley 6430 sub-femtoampere source–measure unit. The carbon electrodes had a diameter of 0.6 cm and their thickness, of about 0.3 mm, was determined as the average value of ten measurements using a Keyence LK-G32 non-contact profilometer. Electric contacts were ensured by copper wires glued with silver paint to the opposite faces of the samples. The imposed current was chosen in the range for which Ohm's law was strictly obeyed, and the measurements were systematically corrected for thermoelectric effect.

Contact angle of the carbon electrodes with the 2 mol L^{-1} H_2SO_4 electrolyte was measured at room temperature with a Krüss DSA 100 Drop Shape Analyser.

Results and discussion

Physicochemical characterisation

The nitrogen adsorption-desorption isotherms of the materials were type-IV and exhibited H4-type hysteresis loops above relative pressure of about 0.4, characteristic of capillary condensation in mesopores (Fig. 1). H4-type hysteresis loops are generally associated with either slit-like pores, particles with internal voids of irregular shape and broad PSDs, or hollow spheres with walls composed of ordered mesoporous silica [27]. The carbons displayed broad PSDs in the micropore region, up to 2 nm, and narrow PSDs in the mesopore region, between ~3 and 4 nm. Increasing the pyrolysis temperature from 800 to 900 °C produced a decrease of surface area, except for PNiH900, and the corresponding increase of the mesoporous fraction of the directly pyrolysed samples of both series (Table 1). This can be explained by the release of volatile matters and the resultant higher relative amount of metal in the final material. The samples PNiH900 and PFeD800 exhibited the highest BET areas, 210 and 220 m^2 g^{-1}, respectively, and PNiH900 and PFeD900 presented the highest mesopore fractions of each series, 66.4 and 78.3%, respectively. Moreover, the presence of narrow porosity in the carbons was negligible, as the values of A_{BET} and S_{QSDFT} were similar to each other. The phthalocyanine–derived materials presented BET areas similar to those or Fe–containing carbon spheres obtained by HTC (200 °C, 3 h) of olive stones in the presence of iron salts (with Fe / C molar ratio of 0.05), and subsequently pyrolysed at 600–800 °C [28].

The materials carbonised at 800 °C presented higher total yields than those carbonised at 900 °C, in agreement with the loss of volatiles at higher temperatures. The total yields, η, were higher for the materials obtained from the nickel phthalocyanine than those derived from the iron phthalocyanine, and the treatment of the precursors by HTC had a different effect depending on the metal: the preliminary HTC increased the total yield of the material obtained from nickel phthalocyanine, PNiH900, with respect to the material directly pyrolysed, PNiD900, while it was lower for the equivalent materials obtained from iron phthalocyanine, PFeH900 and PFeD900, respectively. According to these results, the influence of HTC on the porosity of the materials was different, depending on the metal phthalocyanine used as precursor.

X-ray diffraction (XRD) was used to identify the crystal phases of the materials, and the corresponding patterns are displayed in Fig. S1 (Supporting Information). The samples of the PNi series were very similar to each other, exhibiting elemental nickel and graphite, irrespective to the synthesis method used. It suggests that Ni(II) phthalocyanine was decomposed into NiO and carbon, and that NiO was subsequently reduced by carbon into elemental nickel at high temperature [29,30]. The PFe series samples exhibited graphite and metallic iron, but also various iron carbides and oxides, depending on the synthesis method used. Thus PFeH900, prepared by HTC + pyrolysis, exhibited Fe_2O_3 (maghemite) and $C_{0.12}Fe_{1.88}$ (martensite), while PFeD800 and PFeD900, prepared by direct pyrolysis, presented Fe_3C (cohenite). The formation of iron oxides and iron carbides is indeed normally favoured by HTC, as evidenced by other works [28].

The quantification of the different crystalline phases of PNiH900 and PFeH900 was carried out through Rietveld's refinement using the TOPAS software, and the results are shown in Fig. S2 (Supporting Information section). The metal composition was 25.2% Ni and 13.9% Fe for PNiH900 and PFeH900, respectively, and the crystal size of both metals was very similar, 59 and 64 nm, respectively, indicating that both materials were obtained in similar conditions. Graphite exhibited two contributions: trigonal graphite (C graphite-3R) and hexagonal graphite (C graphite-2H). Interestingly, PNiH900 exhibited a higher amount of trigonal graphite than hexagonal graphite, 43.3 and 31.5%, respectively. This is a very uncommon fact since it is well known that trigonal graphite usually appears as a minor phase in graphitic carbons and mainly in those that have being damaged by milling. The major component in PNiH900 was graphite, while the major components in PFeH900 were iron-based phases (Fig. S2). This suggests that iron exerted a higher catalytic effect towards the gasification of carbon, as confirmed by TG analysis (see below). Still, the crystal size of trigonal and hexagonal graphite in PFeH900 was higher than in PNiH900, suggesting also the higher efficiency of iron than nickel for carbon graphitisation. This was confirmed by Raman spectrometry (see below). For both PFeH900 and PNiH900, however, the crystallite size of trigonal and hexagonal graphite was very low, indicating the nearly absence of long-range order in these carbon materials.

The d_{002} values of the PNi series samples calculated from the peak located at around 26.2°, which is assigned to hexagonal graphite, were 0.342, 0.339 and 0.336 nm for PNiD800, PNiD900 and PNiH900, respectively (Fig. S3 in Supporting Information). For the samples of the PFe series, PFeD800, PFeD900 and PFeH900, the d_{002} values were 0.340, 0.339 and 0.338 nm, respectively. Therefore, the samples directly heated from 800 to 900 °C were slightly more graphitic, as expected, and even more so when prepared by HTC + subsequent pyrolysis at 900 °C since the values of d_{002} values of PNiH900 and PFeH900 were the closest to that of graphite, 0.335 nm.

The TG and DTG curves in argon or air of the samples prepared by HTC are shown in Fig. S4a and S4b, respectively. The pyrolysis of the hydrochars obtained from the Ni(II) and Fe(II) phthalocyanines in argon gave rise to 3 and 5 main weight loss steps, respectively. The progressive sublimation of α-phase into β- phase phthalocyanines might occur up to 550 °C [31,32]. In the case of iron phthalocyanines, for example, a mixture of α-and β-polymorphic states normally exists up to ~400 °C, the α-state progressively disappear-

Table 1
Textural parameters and total yields of the studied carbons.

Sample	A_{BET} [m^2/g][a]	S_{QSDFT} [m^2/g][b]	V_{QSDFT} [cm^3/g][c]	$V_{<0.7}$ [cm^3/g][d]	$V_{0.7-2}$ [cm^3/g][e]	$V_{\mu-N2}$ [cm^3/g][f]	$V_{\mu-CO2}$ [cm^3/g][g]	V_M [cm^3/g][h]	% V_{micro} [Vol.%][i]	% V_{meso} [Vol.%][j]	η [%][k]
PNiD800	196	218	0.15	0.03	0.03	0.08	0.06	0.09	42.63	57.37	58.75
PNiD900	178	193	0.16	0.02	0.03	0.07	0.04	0.11	33.56	66.44	35.79
PNiH900	220	239	0.20	0.03	0.03	0.09	0.05	0.14	32.15	67.85	38.33
PFeD800	210	213	0.14	0.02	0.06	0.08	0.05	0.07	52.40	47.60	37.73
PFeD900	171	168	0.18	0.01	0.03	0.06	0.04	0.14	21.69	78.31	30.14
PFeH900	188	186	0.19	0.01	0.04	0.07	0.03	0.14	27.58	72.42	26.17

[a] A_{BET} = specific surface area calculated through BET equation;
[b] S_{QSDFT} = specific surface area calculated by applying the Quenching Solid Density Functional Theory (QSDFT) to the nitrogen isotherms;
[c] V_{QSDFT} = total pore volume calculated by applying the QSDFT to the nitrogen isotherms;
[d] $V_{<0.7}$ and
[e] $V_{0.7-2}$ = volume of micropores with size lower than 0.7 nm and between 0.7 and 2 nm, respectively, calculated by applying the QSDFT to the nitrogen isotherms;
[f] $V_{\mu-N2}$ = micropore volume calculated by applying the Dubinin – Radushkevich (DR) equation to the nitrogen isotherms;
[g] $V_{\mu-CO2}$ = micropore volume calculated by applying the Dubinin – Radushkevich (DR) equation to the carbon dioxide isotherms;
[h] V_M = mesopore volume calculated as $V_{QSDFT} - (V_{<0.7} + V_{0.7-2})$;
[i] % V_{micro} = percentage of micropore volume;
[j] % V_{meso} = percentage of mesopore volume;
[k] η = total yield.

ing as the temperature increases so that only the β-state remains at ~550 °C [32]. The presence of PFe hydrochar particles, PFe-HTC, exhibiting more defects and/or lower size than those of the PNi hydrochar, PNi-HTC, can contribute to the higher weight loss of the former compound up to 450 °C [32]. The highest weight loss up to 550 °C is due to the transport in vapour phase of phthalocyanines and possibly to the loss of a few volatile matters, between ~200–300 °C, which are swept out to the cold part of the reactor. This weight loss is higher for PFe-HTC than for PNi-HTC, 29.4% and 8.1%, respectively [33,34]. The weight losses above 500–550 °C are mainly assigned to the release of nitrogen groups and non-aromatic hydrocarbons, due to the break-up of the phthalocyanine phenyl rings [32], and the reduction of metallic ions to elemental metals may also take place above 600 °C [28]. 59.3 wt% of the initial weight of PNi-HTC remained at 900 °C whereas 38.8 wt% remained for PFe-HTC. As indicated above, the carbonisation yields of the samples were 50.2 and 34.2%, respectively. Both values differ by 15.3 and 11.9%, respectively, mainly due to the process of vapour phase transport, which takes place in a greater extent when submitting the materials to carbonisation in the quartz reactor located inside the tubular oven flushed by inert gas than in the small crucible of the TG instrument.

The TG and DTG curves in air showed two weight loss steps at 400–600 °C for PNi-HTC and at 450–680 °C for PFe-HTC, which correspond to the decomposition and oxidation of the phthalocyanine structure [35]. PNi-HTC was more reactive towards the oxidising atmosphere, since the initial decomposition temperature was lower than for PFe-HTC [4]. It has been demonstrated that the central metal greatly influences the catalytic properties of the phthalocyanine complexes towards thermal oxidation reactions, and Ni seems to catalyse such decomposition in air faster than Fe [36]. The remaining weight fraction of the final products were 20.6 and 21.6 wt% at 900 °C for PNi-HTC and PFe-HTC, respectively, corresponding to more or less stoichiometric nickel and iron oxides [28].

SEM pictures show that the phthalocyanine-derived materials were composed of particles with irregular size and shape that were highly agglomerated, making it difficult to determine an average particle size (Fig. S5 of Supporting Information). EDX analysis was performed in at least 12 points of each sample, see Figs. S6 and S7 of the Supplementary Information. As expected, carbon was the main element for all materials, with a range of about 91–96 at.%. PNiD800 and PFeD800 presented average contents of 3.30 and 1.15 at.% N, 2.03 and 2.18 at.% O, and 2.71 at.% Ni and 2.00 at.% Fe, respectively. The oxygen concentrations slightly increased for the samples directly pyrolysed at 900 °C and for those prepared through HTC + pyrolysis at 900 °C, 2.25 ± 0.16 and 3.24 ± 0.96 at.% O, respectively; however, the nitrogen concentrations considerably decreased down to 0.82 ± 0.78 at.% and 0.97 ± 0.80 at.% N, respectively, and so did the metal concentrations, 0.99 ± 0.34 at.% Ni and 0.55 ± 0.13 at.% Fe, respectively. The chemical distribution of carbon, nitrogen and oxygen was quite homogeneous, while iron and nickel were mainly detected in the core of the particles (Fig. 2). Such a chemical distribution is consistent with the HRTEM images of the materials, which clearly display quasi-spheres of iron or nickel surrounded by a carbon shell having a graphitic structure (Fig. 3). The distance between the corresponding carbon layers was estimated at ~0.34 nm from the inset of Fig. 3, i.e., slightly higher than that of perfect graphite, 0.335 nm, as expected. In both cases, the metal-encapsulated carbon spheres coexisted with onion–like structures and graphitic carbon nanoribbons (Fig. 3a and b). Similar structures have been previously obtained by annealing at 900 °C dehydro[18]annulenes containing a ferrocene cycle [37].

The catalytic effect of iron and nickel on carbon graphitisation above 1000 °C has been widely demonstrated elsewhere, but it seems to be favored even at lower temperatures, 800 and 900 °C, when both metals are intimately mixed with carbon as it is obviously the case in phthalocyanines [28,38]. Undoubtedly, the highly aromatic character of the phthalocyanine structure may contribute to favour the graphitisation of the materials.

The Raman spectra evidenced a first-order part, ranging from 1000 to 1800 cm^{-1}, and a second-order part, ranging from 2200 to 3400 cm^{-1} (Fig. 4). The first-order Raman spectra of the materials treated at the lowest temperature, 800 °C, presented an intense and broad D band and a slightly less intense but narrower G band, typical of disordered carbons. The D bands were centered at 1342.8 ± 1.0 cm^{-1} and 1346.9 ± 0.0 cm^{-1} and the G bands were centered at 1591.1 ± 1.0 cm^{-1} and 1587.2 ± 5.0 cm^{-1} for the PNi and PFe series samples, respectively. The $I(D)/I(G)$ ratios were calculated from the maximum intensities of the D and G bands and were plotted for the two series of samples (Fig. S8 in Supporting Information). The presence of Ni and Fe in contact with carbon is expected to produce the catalytic graphitisation of the latter, and therefore the observed decrease of the $I(D)/I(G)$ ratio indicates that these materials are indeed in the graphitisation regime [39]. In this condition, the $I(D)/I(G)$ ratio is inversely proportional to $1/L_a$, where L_a is the crystallite size along the carbon layers [40]. As expected, increasing the temperature thus logically improved the structural ordering of the carbon at the nanoscale, whether the

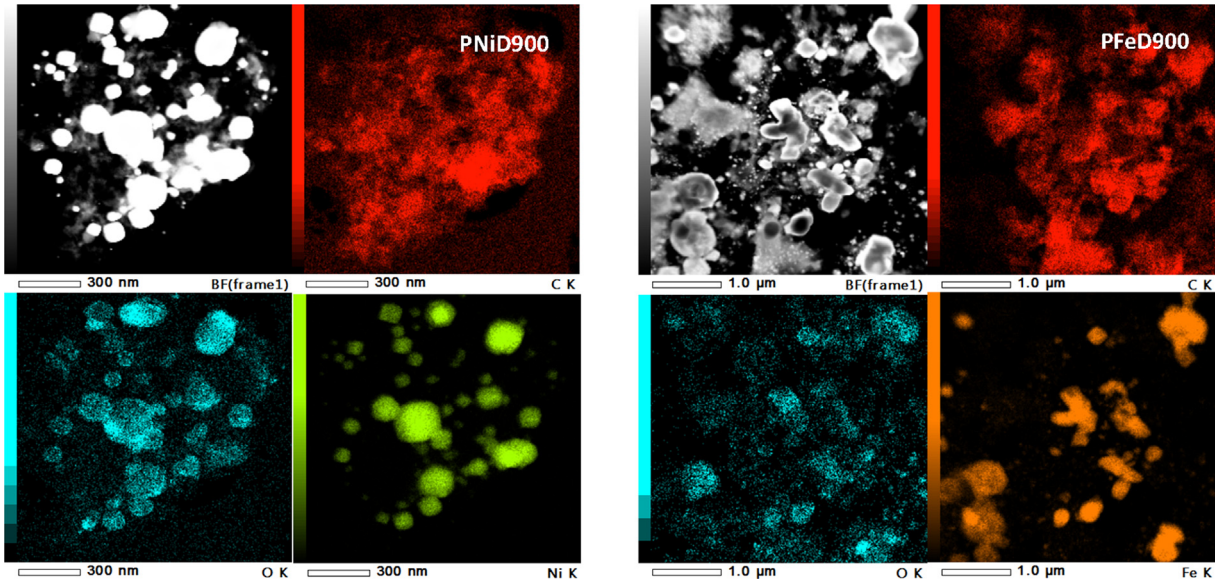

Fig. 2. Chemical mapping of elements (C, O and Ni or Fe) determined by SEM-EDX present in PNiD900 (left) and PFeD900 (right).

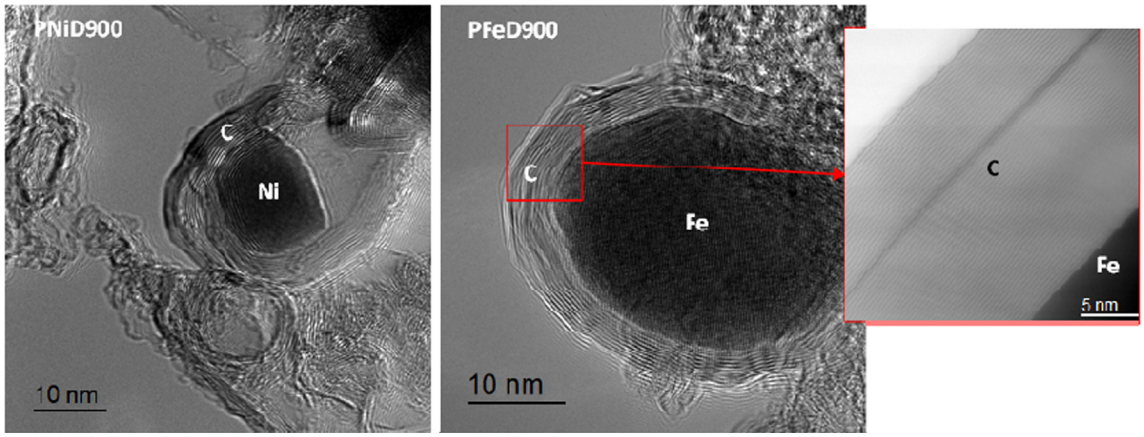

Fig. 3. High-resolution TEM images of PNiD900 (left) and PFeD900 (middle), prepared by direct pyrolysis. The inset at the right is a zoom on the PFeD900 carbon shell.

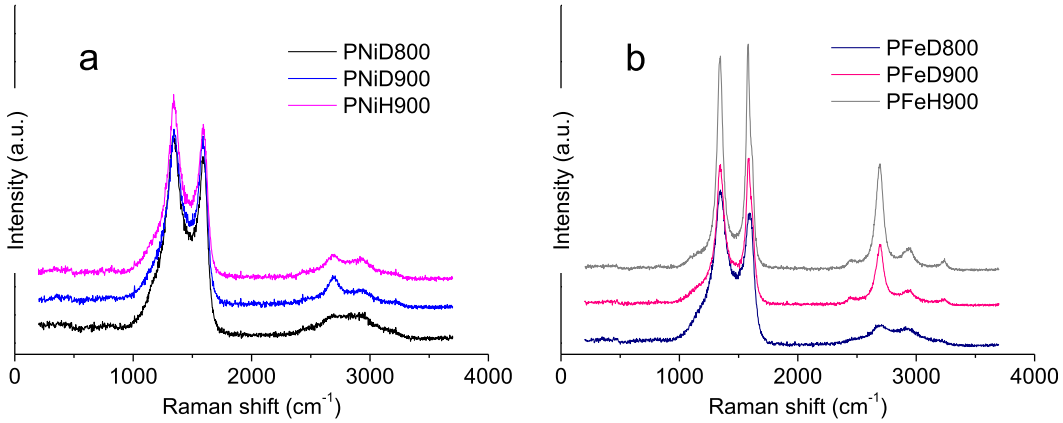

Fig. 4. First- and second-order Raman spectra of the studied materials: (a) PNi series; (b) PFe series. The intensities were normalised with respect to the D band and the spectra were shifted for clarity.

metal was Ni or Fe. In the case of Fe, the preliminary HTC treatment (PFeH900) improved the graphitisation of the PFe series, since PFeH900 presented a lower $I(D)/I(G)$ ratio than PFeD900, in agreement with the lower d_{002} observed from XRD results. It is not clear yet why the hydrothermal treatment had not exactly the same effect on Ni-derived carbons, and it may be conjectured that the

different Lewis acidic character of Ni(II) and Fe(II) played a role when the materials were submitted to hot pressurised water conditions.

Considering the 2nd-order part of the Raman spectra led to the same conclusions as above. The very broad band from ~2500 to ~3300 cm^{-1} of sample PNiD800 was very poorly structured, and such feature is typical of a highly disordered carbon. This band, called S1, is known to split into two bands when the structure of carbon acquires a tri-periodic order [41], i.e., involving an order in the way the carbon layers are stacked. The appearance of two small peaks instead of a broad one in the 2nd-order part of the spectra of PNiH900 and PFeD800 suggests the better organisation of these materials with respect to PNiD800. The carbon nanotexture was even more ordered in PFe samples treated at 900 °C, since the corresponding spectra presented narrow bands and very well defined second-order parts. Especially, the band near 2700 cm^{-1}, called 2D because it is an overtone of band D, which was more developed in PFeH900. This band is assigned to edge planes [42], so that an increase of its intensity is related to a higher degree of graphitisation and indicates the development of a graphitic nanostructure [43]. The growth of the D + D' and 2D' bands near 2930 and 3200 cm^{-1}, respectively, is one more proof of the formation of a defective graphitic nature of PFe samples treated at 900 °C [44]. In summary, Fe-based phthalocyanines always led to more graphitic structures than Ni-based phthalocyanines carbonised at the same temperature, especially when a preliminary HTC step was carried out.

The bulk chemical composition of the materials was determined by elemental analysis (Table 2). Increasing the pyrolysis temperature from 800 to 900 °C for the directly pyrolysed samples produced a slight decrease of nitrogen and oxygen concentrations and an increase of carbon and metal contents. Assuming that metals remain in the materials in this range of temperature, these findings are consistent with the loss of thermally unstable nitrogen and oxygen groups from the surface. Since oxygen is not present in phthalocyanine molecules, the oxygen found in the materials is expected to come from oxidation of carbon defects and edges with air and/or from the impurities of the raw precursors [4]. The samples prepared through HTC + pyrolysis, PNiH900 and PFeH900, exhibited higher amounts of nitrogen and oxygen than the samples directly pyrolysed at 900 °C, PNiD900 and PFeD900. This may indicate the formation of nitrogen and oxygen groups during HTC that are more thermally stable than those formed through direct pyrolysis [45]. Moreover, the amount of metal removed from PNiH900 and PFeH900 by acid etching was higher than for the other samples, likely indicating that the metal was more accessible.

Very low concentrations of metals were detected by XPS at the surface of the materials (Table S1 in Supporting Information). The surface concentration of nickel was 0.2–0.3 at. % in the PNi series, and that of iron was 0.1–0.4 at.% in the PFe-derived samples. The respective signals for both metals were so weak that the quantification was inaccurate, and the surface concentrations might thus be even lower. In the case of iron, for example, the curve fitting was impossible for PFeD800 and PFeD900. Given that nickel concentrations up to 17.9 wt% (4.0 at.%) and iron concentrations up to 20.0 wt% (4.81 at.%) were measured in the material bulk, the low metal concentrations found at their surfaces clearly indicates that both metals are encapsulated inside carbon shells [46], as already seen in Fig. 4.

Fitting the Ni2p region for PNiD800 and PNiD900 was also very inaccurate due to the high nitrogen content of the samples, 3.6 and 2.1 at.%, respectively: the signal of the Auger electrons of nitrogen was indeed very strong and interfered with the signal of $Ni2p^{1/2}$, located in the same region. In the case of PNiH900, fitting the $Ni2P^{1/2}$ region was more accurate because the N concentration was lower, ~1.3 at.%, and the signal of Auger electrons of nitrogen did not interfere so strongly. Thus, only the relative intensity factors of $Ni2p^{3/2}$ were considered to fit the Ni2p high-resolution spectra of PNiD800 and PNiD900, and the relative intensity factors of $Ni2p^{1/2}$ and $Ni2p^{3/2}$ were considered to fit the Ni2p high-resolution spectra of PNiH900.

The fitting of the peaks revealed the presence of various contributions for the $Ni2p^{3/2}$ region (Fig. S9 in Supporting Information). The corresponding binding energies, BE (eV), and relative areas, A (%), are given in Table S1 (Supporting Information). The Ni2p high-resolution spectra of PNiD800 and PNi900 presented the peaks II(1), assigned to Ni^0; II(2), assigned to NiO; and III(3), assigned to Ni-C complexes. No shake-up peak was obtained despite the presence of NiO, which can be due to the low surface concentration of nickel. In the case of PNiH900, the existence of the shake-up peak evidenced the presence of oxidised nickel species, NiO and Ni-C. No Ni^0 was found for this sample. The Ni-C peak is assigned to a Ni-C complex but also to Ni_2O_3; the latter is highly unstable and may originate from the oxidation of Ni(II) by the XPS radiation [47]. Two oxidised Ni species were thus identified by XPS on the surface of the PNi series samples, but only Ni^0 was identified by XRD. These observations are not contradictory, since XRD gives information about the material bulk and only detects crystallised compounds, whereas XPS investigates the material surface and its sensitivity is higher than that of XRD.

The Fe2p high-resolution spectrum of PFeH900 exhibited complex multiplet splitting and presented satellite features, which allowed determining the oxidation states of iron (Fig. S9 in Supporting Information). Due to the low intensity of the emission line, the $Fe2p^{3/2}$ region of the spectrum was only fitted by two peaks and the shake-up satellite, instead of the six peaks that can be normally used for Fe^{3+} and appearing at this BE [48]. The two peaks obtained, II(1) and II(2), indicate the presence of Fe(III), likely in the form of Fe_2O_3 [49].

The Ni2p and Fe2p high-resolution spectra are consistent with the O1s high-resolution spectra of the samples (Fig. S10 in Supporting Information). The latter indeed presented three contributions: O(1) peak, assigned to metal-oxygen bonds in metal oxides [49,50]; O(2) peak, assigned to C═O double bonds in quinone-type groups, carbonyls and carboxylic acids; and O(3) peak related to —OH bonds in phenols, to C—O—C ether groups and to C═O

Table 2
Chemical composition of the materials obtained by elemental analysis.

Sample	Elemental Analysis [wt%]						
	C	N	O	H	S	Metal*	Metal removed*
PNiD800	79.51	4.45	4.58	0.45	0.00	11.60	3.21
PNiD900	88.82	2.57	3.27	0.24	0.00	5.28	11.04
PNiH900	85.55	3.57	4.02	0.33	0.00	6.48	11.39
PFeD800	85.52	2.37	5.07	0.32	0.00	8.30	5.66
PFeD900	94.59	0.83	2.67	0.11	0.00	2.66	11.77
PFeH900	89.17	1.80	4.39	0.31	0.03	4.00	15.95

* Calculated by difference.

bonds in ester and anhydride groups [51]. The assignations for the peaks of the C1s and N1s high-resolution spectra are typical of carbon materials (Figs. S11 and S12 in Supporting Information), and can be found in Table S1 (Supporting Information). In general, the most abundant nitrogen groups on the material surface were pyridinic (N6 peak), pyrrolic (N5 peak) and quaternary nitrogen (NQ peak). Samples prepared with the same procedures exhibited interesting chemical similarities: PNiD800 and PFeD800 possessed the highest amounts of N6 and N5, PNiH900 and PFeH900 the highest amounts of metal-oxygen compounds, and PNiD900 and PFeD900 the highest amounts of NQ. Although the concentration of carbonyls and quinones was not very different among the studied carbons, PNiD900, PFeD800 and PFeH900 exhibited the highest concentrations.

From the above results, it was confirmer that both nickel and iron are essentially located in the core of carbon particles, in other words, are encapsulated. Nickel is mainly in the form of Ni^0, but iron is found simultaneously in the form of Fe^0, iron oxides and iron carbides. The low concentrations of nickel and iron that can be detected on the material surface are partially oxidised.

Electrochemical characterisation

Cyclic voltammetry (CV) tests were performed in a two-electrode cell at scan rates between 1 and 1000 mV s^{-1} within the potential window of 0–1 V and using 2 mol L^{-1} H_2SO_4 as electrolyte. The specific capacitance of the two-electrode system (*C2e*, F g^{-1}) was calculated from the CV curves according to Eq. (1):

$$C2e = \left(\int I\Delta V\right)/(s\Delta Vm) \quad (1)$$

where I (A) is the current, s (V s^{-1}) is the scan rate, ΔV (V) is the potential window and m (g) is the mass of carbon in the electrodes. The gravimetric capacitance for a single electrode (*C3e*, F g^{-1}) can be estimated through Eq. (2):

$$C3e = 4 \times C2e \quad (2)$$

The CV curves and the results of specific capacitance of the studied electrodes are shown in Fig. S13 (Supporting Information). The CV curves presented quasi-rectangular shape in the entire range of scan rates, with no obvious redox peaks associated to Faradaic reactions of the surface groups (Fig. S13a–b). This suggests that the energy was mainly stored by an electric double-layer capacitance (EDLC) mechanism, i.e., based on ion adsorption. When the scan rate increased from 1 to 1000 mV s^{-1}, the CV curves of the PNi–derived electrodes became somewhat distorted but still retained a rectangular shape (Fig. S13a). In the case of the PFe–derived electrodes, the CV curves had a rectangular shape for PFeH900 and PFeD900, but were highly distorted for PFeD800. The rectangular shape of the curves at the highest scan rate of 1 V s^{-1} indicates a fast ion transport and high rate capability of the samples, which is of great importance for practical devices. The highly distorted CV profile of PFeD800 suggests that this sample exhibits the highest ion transport resistivity and the lowest rate capability out of all present materials.

The values of specific capacitance at the lowest scan rate of 1 mV s^{-1} seemed to be more related to the preparation method than to the type of metal phthalocyanine. PNiD800 and PNiH900 exhibited the highest capacitances of ~14 F g^{-1} (*C3e* = 56 F g^{-1}), followed by PFeD800 and PFeH900, ~13 F g^{-1} (*C3e* = 52 F g^{-1}). However, PNiD900 and PFeD900 displayed the lowest specific capacitances of their respective series, 11 and 6 F g^{-1} (*C3e* = 44 and 24 F g^{-1}) (Fig. S13c–d). On the contrary, the capacitance retention values at the highest scan rate of 1 V s^{-1} seemed to be more related to the type of phthalocyanine. The PFe series carbons exhibited the highest capacitance retentions of 73.0 and 72.4% for PFeD900 and PFeH900, respectively, with the exception of PFeD800 that attained only 36.8% (Fig. S13f). These values were a bit smaller for the PNi-derived materials, which exhibited capacitance retentions between 56.0 and 61.7% for PNiH900 and PNiD800, respectively (Fig. S13e).

Galvanostatic charge–discharge (GCD) experiments were studied in a two-electrode cell within the potential window 0–1 V. The GCD curves were obtained at current densities between 0.2 and 12 A g^{-1}, based on the total mass of the two electrodes. From these measurements, the gravimetric capacitance, *C2e* (F g^{-1}) was calculated by applying Eq. (3):

$$C2e = I/[m(dV/dt)] \quad (3)$$

where I (A) represents the discharge current, dV/dt (V s^{-1}) is the slope of the discharge curve without considering the voltage drop, *IR* (V), due to the inner resistance at the beginning of the discharge process, and m (g) is again the mass of carbon in both electrodes.

In general, the GCD curves of the samples exhibited quasi-triangular profiles typical of carbon materials, thus indicating that ion storage mainly occurred through an EDLC mechanism (Fig. 5a–b). However, the GCD curve of PFeD800 slightly deviated from the triangular shape, especially the discharge curve, and this could indicate the occurrence of a pseudocapacitance contribution to the total capacitance. The GCD curves recorded at 5 A g^{-1} exhibited a sudden potential drop, or *IR* drop, at the beginning of the discharge process, which is attributed to the cell resistance, R_{cell} (Fig. 5–b). The values of specific capacitance at the lowest current density of 0.2 A g^{-1} were also more related to the preparation method than to the type of metal phthalocyanine (Fig. 5c–d). PNiD800 and PNiH900 displayed the highest capacitances of the PNi series, 15 F g^{-1} (*C3e* = 60 F g^{-1}) and 12 F g^{-1} (*C3e* = 48 F g^{-1}), respectively, and PFeD800 and PFeH900 the highest ones of the PFe series, 14 F g^{-1} (*C3e* = 56 F g^{-1}) and 12 F g^{-1} (*C3e* = 48 F g^{-1}), respectively. Moreover, PNiD900 and PFeD900 also presented the lowest specific capacitances of their respective series, 9 F g^{-1} (*C3e* = 36 F g^{-1}) and 6 F g^{-1} (*C3e* = 24 F g^{-1}), respectively. The decrease of capacitance with increasing current densities is due to the increasing ohmic resistance of the electrolyte in the axial direction of the micropores (Fig. 5c–d). This is related to the increased potential difference between the mouth and the bottom of the micropores as the current density increases, thus decreasing the ion diffusion in the micropores [52]. Among the studied materials, PFeD900 and PFeH900 yielded the highest capacitance retentions of 80.0 and 84.5%, respectively, at the highest current density of 12 A g^{-1}. The PNi–derived electrodes exhibited capacitance retentions between 60.5 and 77.6% for PNiD800 and PNiH900, respectively, and PFeD800 presented the lowest capacitance retention out of all materials, 36.5%. These results are in agreement with those obtained from the CV tests, discussed above.

The energy density, E (Wh kg^{-1}), and the power density, P (W kg^{-1}), were calculated from the GCD tests at current densities ranging from 0.2 to 12 A g^{-1} by applying Eqs. (4) and (5), respectively:

$$E = 1/2\ C2e\ \Delta V_{d^2} \quad (4)$$

$$P = E/\Delta t_d \quad (5)$$

where *C2e* (F g^{-1}) represents the specific capacitance calculated from Eq. (3) that considers the carbon mass in the two electrodes, ΔV_d (V) is the operation voltage calculated as $V_{max} - IR$, where *IR* (V) is again the voltage drop due to the inner resistance at the beginning of the discharge process, and Δt_d (s) is the discharge time. The cycling stability was also studied through GCD tests at the current density of 5 A g^{-1} up to 10 000 cycles of charge–discharge. The

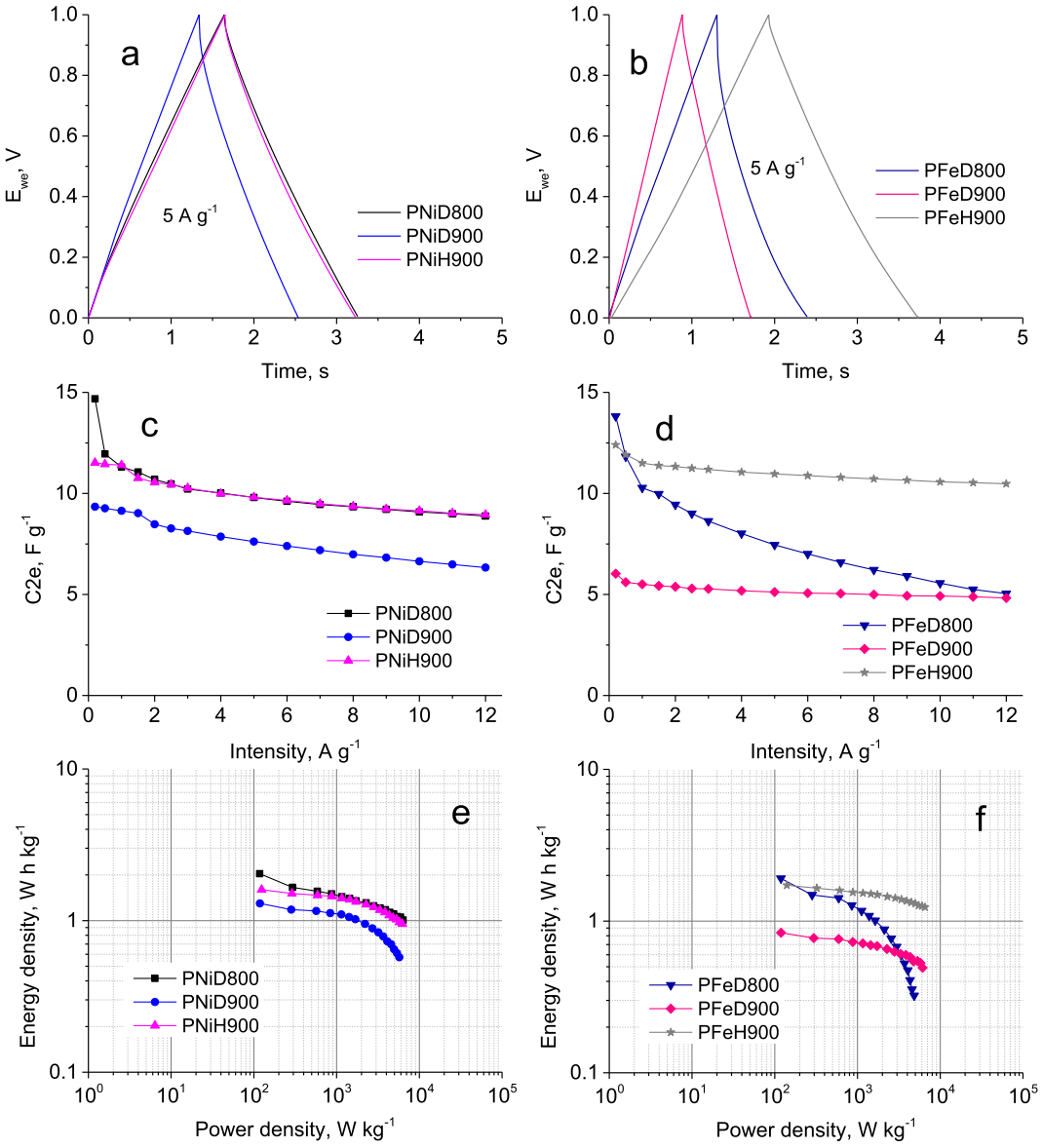

Fig. 5. Galvanostatic charge–discharge (GCD) results obtained with 2 mol L^{-1} H_2SO_4 electrolyte within the potential window 0–1 V: (a,b) GCD curves recorded at 5 A g^{-1}; (c, d) Specific capacitance values from 0.2 to 12 A g^{-1}; (e,f) Ragone plots.

specific capacitance for a given GCD cycle and the capacitance retention were determined by using Eq. (3).

As expected, the samples exhibiting the highest capacitances determined by GCD presented the highest energy densities, that is, PNiD800 and PNiH900, and PFeD800 and PFeH900 (Fig. 5e–f). Among the studied materials, PFeH900 exhibited the highest energy and power densities in the entire range of current densities: the energy densities varied in the range of 1.7–1.2 W h kg^{-1} under the power outputs of 140.3–6537.5 W kg^{-1}, respectively. PFeD800 presented high energy density at low current, but it sharply decreased above 1 A g^{-1}, as well as the power densities, and PNiD900 and PFeD900 presented the lowest energy and power density values of both series.

In a general way, the capacitance values obtained by CV and GCD, and then the energy densities obtained by GCD, can be explained in terms of the S_{QDFT} values, since both parameters are directly related. PNiD900 is an exception, given that it should yield at least a similar capacitance to that of PFeH900, according to its surface area. The capacitance retentions can be related to the mesopore fraction, % V_{meso}, of the materials. It is generally accepted that mesopores facilitate diffusion of electrolyte ions towards micropores, thus increasing the capacitance retention both at high scan rates and at high current regimes. In this sense, the sharp capacitance decrease of PFeD800 when both scan rates and current densities increase can be mainly attributed to its low mesopore fraction of 37.7%. However, the capacitance retention of PFeD900 should be higher than that of PFeH900, according to its higher mesopore percentage of 78.3%.

In order to clarify these observations, the *IR* drop of the materials was calculated from the GCD curves obtained at current densities between 0.2 and 12 A g^{-1}. The cell resistance was determined through the slope of the straight lines obtained by plotting the *IR* drop as a function of discharge current (Fig. S14a–b in Supporting Information). Interestingly, there is a clear relationship between R_{cell} and energy and power densities of the electrode materials: the samples displaying the highest cell resistances, PNiD900, PFeD800 and PFeD900, also presented the lowest energy and power density values, especially at high current. PNiD800 and

PNiH900 exhibited similar cell resistances R_{cell} and, consequently, similar E and P densities, and PFeH900 exhibited the lowest R_{cell} and the highest E and P densities out of all materials. R_{cell} comprises the electrolyte resistance, the intrinsic resistance of the active material, and the interfacial contact resistance between the active material and the current collector [53]. As the same electrolyte was used in all cases, the observed differences should be mainly explained by differences in the intrinsic resistance of the carbon electrodes and in the interfacial contact between the active material and the current collector. It is well known that the electrical conductivity of the carbon electrodes is a key parameter to enhance the charge transfer between the electrode and the current collector, thus leading to an improvement of the energy and power density of the supercapacitor [54]. Surprisingly, PNiD900 and PFeD900 electrodes presented the highest electrical conductivities, 0.53 and 0.43 S cm^{-1}, respectively, but their capacities and energy densities were the lowest of both series (Fig. S15 in Supporting Information). In principle, it is expected that electrical conductivity is affected by oxygen moieties due to their electron-withdrawing nature [55,56], but no conclusive data have been published so far. For example, on the one hand, the removal of hydroxyl and epoxide groups from the basal plane of potentially insulating GO has been related to an increased electrical conductivity [57,58]. But, on the other hand, the presence of low concentrations of oxygen groups on carbon blacks, such as in the present study, was proved to have a very limited influence on the electrical conductivity [59]. Regarding the nitrogen groups, the general consensus concludes to the enhancement of the electrical conductivity by NQ groups, since each of them gives ~0.5 electrons to the π network of the carbon lattice, which can be considered as n-type doping. Nevertheless, it has been recently observed that the coexistence of electron-accepting N6 and N5 moieties with electron-donating NQ ones, may weaken the n-doping effect of NQ by reducing the electron mobility with respect to pristine graphene, thus in turn decreasing the electrical conductivity [60]. Consequently, the values of electrical conductivity of the studied samples may be mainly attributed to the combination of the graphitisation degree of the carbon materials and of the relative amounts of N6, N5 and NQ moieties. It may also be recalled that PNi-derived samples contained elemental metal, whereas those of the PFe series were also rich in oxides, thus decreasing their conductivity further. PNiD900 and PFeD900 yielded the highest conductivity values due to their high graphitic character, low N6 and N5 concentrations, and high NQ concentrations, while the opposite situation occurred in the case of PNiD800 and PFeD800. A denser packing of the carbon particles or a higher obstruction of the pore entrance by PTFE binder in PNiD900 and PFeD900 may hinder the ion transport through the electrodes and increase R_{cell}, despite possessing higher electrical conductivities than the other materials. This fact, together with their low surface areas and their comparatively lower concentrations of electroactive groups, such as N6 and N5, may contribute to the lower capacitances and energy densities of both samples with respect to those of their respective series.

The cycling stability of the samples was exceptionally high, 98 ± 1 and 99 ± 0% for the PNi and PFe series, respectively, at 5 A g^{-1} up to 10 000 cycles of charge-discharge (Fig. S14c–d). R_{cell} slightly increased with the number of cycles for all the samples (Fig. S15e), but the energy and power densities remained essentially the same throughout the 10 000 cycles of charge-discharge at 5 A g^{-1} (Fig. S14f). It is noteworthy that the cycling stabilities of the materials published in this work are similar than those reported for 3D CNT–supported graphene nanoarchitectures exhibiting higher BET areas of 418 m^2 g^{-1}, which yielded capacitance retentions of ~98% after 10 000 cycles of charge-discharge in 1 M H_2SO_4 [61]. Clew–like porous carbons obtained by catalytic graphitisation of sucrose with nickel acetate and submitted to further activation attained lower capacitance retentions of 86.6–94.3% after 5000 cycles at a lower current density of 0.5 F g^{-1} in 6 M KOH, despite possesing higher surface areas up to 691 m^2 g^{-1} [62]. Mesoporous carbon microspheres obtained from resorcinol–formadehyde resins through catalytic graphitisation with nickel nitrate at 900 °C and subsequent activation also exhibited much lower capacitance retentions of ~90% after only 500 cycles of charge-discharge at lower current densities of 1 A g^{-1} and using 6 M KOH as electrolyte, whereas their BET areas were higher than 1000 m^2 g^{-1} [29]. It is also remarkable that, while the synthetic processes applied to prepare these materials are complicated, use hazardous precursors or need activation to further develop their porosities, the materials synthesised in the present work were simply obtained from phthalocyanines by direct carbonisation or by HTC in water + carbonisation without any activation step.

Interfacial capacitance was used to estimate the participation of surface groups to the total capacitance through pseudocapacitance, the latter being proportional to the surface heteroatom concentration. The interfacial capacitances of the materials were calculated by dividing the specific capacitances obtained at different scan rates by the surface areas obtained by application of the QSDFT method, C/S_{QSDFT} [14]. The samples directly carbonised at 800 °C, PNiD800 and PFeD800, exhibited the highest interfacial capacitances of their respective series in the entire range of scan rates, while PNiD900 and PFeD900 exhibited the lowest ones (Fig. 6a–b). This suggests that the surface chemistry of the materials contributes to the total capacitances through the occurrence of Faradaic reactions at the electrode surface, which allows storing the energy through a pseudocapacitance mechanism. The values of C/S_{QSDFT} at different scan rates were plotted versus the content of the different groups observed at the material surface, and the best correlation was found with the concentration of N + O surface groups (Fig. 6c–f). Among the nitrogen groups, N6 and N5 contributed to increase the capacitance of the materials through pseudocapacitance (Fig. S16a–b in Supporting Information), as well as the oxygen groups determined by O(2) and O(3) (Fig. S16c–d in Supporting Information). The correlation between the interfacial capacitances and the amount of metals was not conclusive. Considering that metals were surrounded by carbon, and given the extremely low metal concentration observed at the materials' surface, it is highly probable that the contact of metal with electrolyte is negligible so that they can never contribute to the capacitance through Faradaic processes. Metal encapsulation by carbon has proved to be highly effective to prevent the degradation of the metal by the electrolyte during the cycling life of the derived supercapacitors, as evidenced by the extraordinary high capacitance retentions attained by the phthalocyanine-derived materials after 10 000 cycles of charge–discharge. Interfacial capacitances defined as the ratio C/A_{BET} were also calculated for comparison with previously reported data (Fig. S17 in Supporting Information). The phthalocyanine–derived materials yielded higher interfacial capacitances than those attained not only by materials with similar BET areas, such as iron–catalysed graphitic mesoporous carbons in 6 M KOH electrolyte [24] or iron–catalysed biomass–derived carbons in 1 M KOH electrolyte [63], but also by materials with much higher BET areas, such as activated carbon aerogels in 30% KOH electrolyte (A_{BET} = 1418 m^2 g^{-1}) [64], nickel–catalysed graphitic activated carbons in 1 M H_2SO_4 electrolyte (A_{BET} = 1558–1622 m^2 g^{-1}) [65] or nickel–catalysed mesoporous carbon microspheres in 6 M KOH electrolyte (A_{BET} = 1088–1096 m^2 g^{-1}) [29]. The pseudocapacitance contribution of the surface groups through Faradaic reactions and the graphitic character of the materials contribute decisively to the comparatively higher electrochemical performances of the phthalocyanine-derived carbons.

The different concentrations of N and O groups of the carbons had no obvious effects on the wettability of the electrode surfaces

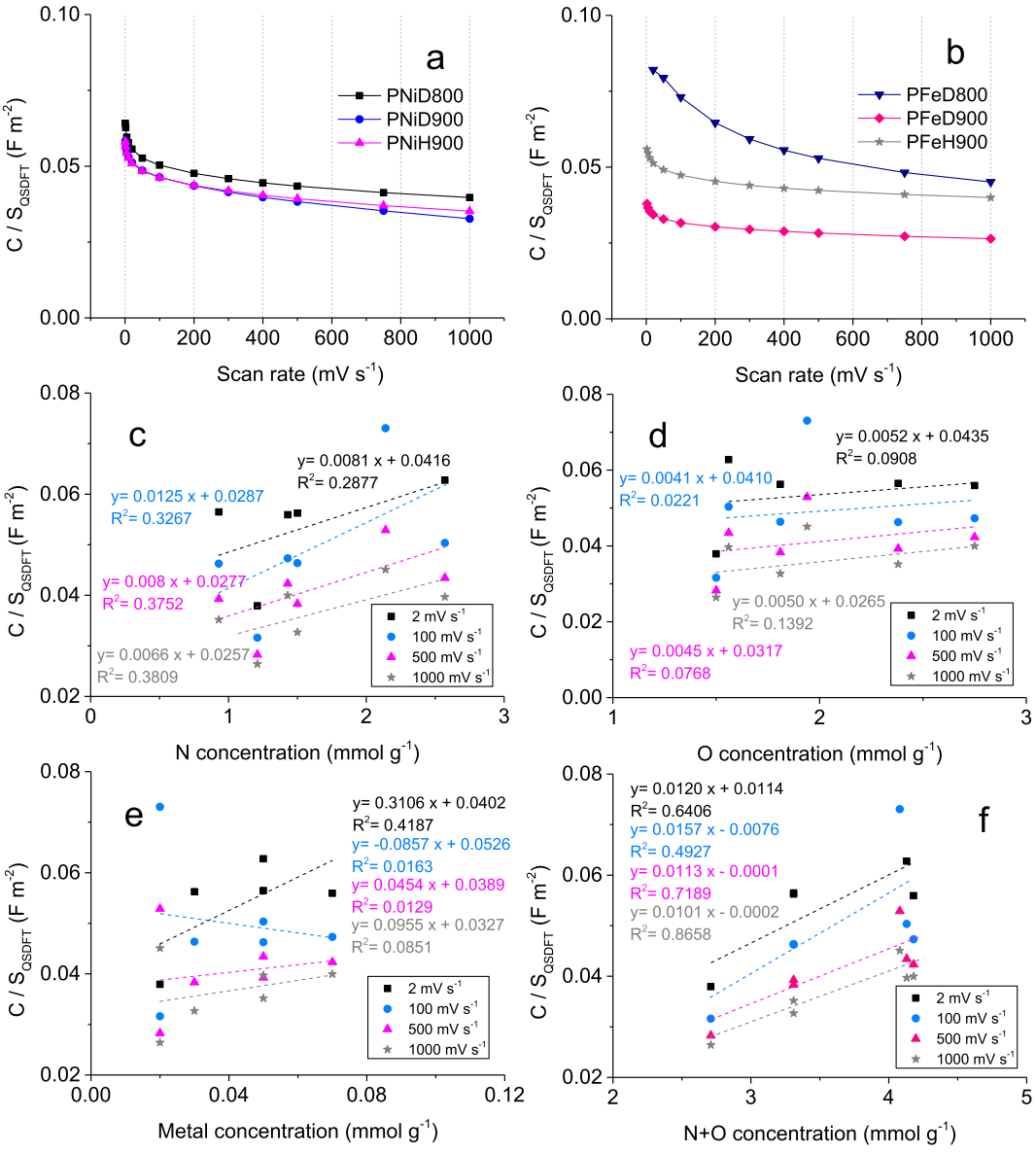

Fig. 6. (a,b) Interfacial capacitance, C/S_{QSDFT}, obtained from CV curves at scan rates between 1 and 1000 mV s^{-1}; (c–f) Interfacial capacitance vs surface concentration of heteroatoms (N, O, metal, and N + 0).

by the electrolyte, 2 mol L^{-1} H_2SO_4, since the contact angle was higher than 90° in all cases (Fig. S18 in Supporting Information). This means that the interaction of the electrodes with the electrolyte was hydrophobic, which agrees with the graphitic character of the carbons and their homogeneous mixture with the binder, PTFE. Complete impregnation was therefore guaranteed by keeping the electrodes with the electrolyte during 4 days under vacuum.

Conclusion

Nickel and iron phthalocyanines gave rise to N,O-co-doped carbons having high mesopore fractions, narrow pore size distributions between ~3 and 4 nm, and graphitic carbon structures, by simply carbonising them at 800 or 900 °C, or by submitting them first to HTC in water, followed by pyrolysis at 900 °C. Neither additional N-doping post-treatment or mesoporous templates were required, and low pyrolysis temperatures were enough to obtain graphitic carbon thanks to the presence of Ni or Fe, naturally present in the precursors, and which acted as graphitisation catalysts.

The PNi materials were composed of elemental nickel and graphite, irrespective of the synthesis method used, while the PFe materials contained graphite, metallic iron and various carbides and oxides depending on the synthesis method. Iron seemed to be more effective as catalyst because of the higher size of graphite crystallites and the main presence of iron-based phases in the materials, whereas nickel produced an extraordinarily high level of trigonal graphite, which is generally a minor phase in carbons. In both cases, graphite lacked long-range order and was mainly forming graphitic carbon nanoribbons and onion–like structures.

Both nickel and iron were encapsulated in the core of the onion–like structures, with no contact with the electrolyte and with no effect on energy storage. The studied phthalocyanine-derived carbons presented unusually high cycling stabilities, exhibiting capacitance retentions up to 99% after 10 000 cycles of charge-discharge, and yielded higher electrochemical performances than a wide variety of materials with much higher surface

areas, which is mainly assigned to their graphitic character and to the pseudocapacitance contribution of the surface groups.

Therefore, this work opens a new way to transform a broad range of metal phthalocyanines, their derivatives, as well as other organometallic complexes into graphitic carbon materials.

Compliance with ethics requirements

This article does not contain any studies with human or animal subjects.

Declaration of Competing Interest

The authors have declared no conflict of interest.

Acknowledgements

The IJL research team gratefully acknowledges the Dr. Marta Sevilla's departement for its scientific support, and the financial support of the CPER 2007-2013 "Structuration du Pôle de Compétitivité Fibres Grand'Est" (Competitiveness Fibre Cluster), through local (Conseil Général des Vosges), regional (Région Lorraine), national (DRRT and FNADT) and European (FEDER) funds. Dr. A. Sanchez-Sanchez acknowledges the CNRS for financing her post-Doctoral contract.

Appendix A. Supplementary material

Supplementary data to this article can be found online at https://doi.org/10.1016/j.jare.2019.11.004.

References

[1] Ben-Hur E, Chan W-S. Phthalocyanines in photobiology and their medical applications, vol. 19. Karl M. Kadish; Kevin M. Smith; Roger Guilard; 2012. DOI:10.1016/B978-0-08-092393-2.50007-X.
[2] Dumoulin F, Durmuş M, Ahsen V, Nyokong T. Synthetic pathways to water-soluble phthalocyanines and close analogs. Coord Chem Rev 2010;254:2792–847. https://doi.org/10.1016/j.ccr.2010.05.002.
[3] Jasinski R. A new fuel cell cathode catalyst. Nature 1964;201:1212–3. https://doi.org/10.1038/2011212a0.
[4] Jones JM, Agnew J, Kennedy J, Watts B. Porphyrin- and metalloporphyrin-derived carbons as models for coal char combustion and pyrolysis. Fuel 1997;76:1235–40. https://doi.org/10.1016/s0140-6701(98)94047-4.
[5] Kim NS, Lee YT, Park J, Han JB, Choi YS, Choi SY, et al. Vertically aligned carbon nanotubes grown by pyrolysis of iron, cobalt, and nickel phthalocyanines. J Phys Chem B 2003;107:9249–55. https://doi.org/10.1021/jp0348950.
[6] Huang S, Dai L. Microscopic and macroscopic structures of carbon nanotubes produced by pyrolysis of iron phthalocyanine. ChemInform 2003;34. https://doi.org/10.1002/chin.200321221.
[7] Borgatti-Jeffreys A, Hooser SB, Miller MA, Lucroy MD. Phase I clinical trial of the use of zinc phthalocyanine tetrasulfonate as a photosensitizer for photodynamic therapy in dogs. Am J Vet Res 2007;68:399–404. https://doi.org/10.2460/ajvr.68.4.399.
[8] Chidembo AT, Ozoemena KI, Agboola BO, Gupta V, Wildgoose GG, Compton RG. Nickel(ii) tetra-aminophthalocyanine modified MWCNTs as potential nanocomposite materials for the development of supercapacitors. Energy Environ Sci 2010;3:228–36. https://doi.org/10.1039/B915920G.
[9] Chidembo AT, Ozoemena KI. Electrochemical capacitive behaviour of multiwalled carbon nanotubes modified with electropolymeric films of nickel tetraaminophthalocyanine. Electroanalysis 2010;22:2529–35. https://doi.org/10.1002/elan.201000290.
[10] Walter MG, Rudine AB, Wamser CC. Porphyrins and phthalocyanines in solar photovoltaic cells. J Porphyrins Phthalocyanines 2010;14:759–92. https://doi.org/10.1142/S1088424610002689.
[11] Lee KT, Ji X, Rault M, Nazar LF. Simple synthesis of graphitic ordered mesoporous carbon materials by a solid-state method using metal phthalocyanines. Angew Chem Int Ed 2009;48:5661–5. https://doi.org/10.1002/anie.200806208.
[12] Titirici M-M, Funke A, Kruse A. Hydrothermal carbonization of biomass. Recent Advances in Thermo-Chemical Conversion of Biomass 2015:325–52. https://doi.org/10.1016/B978-0-444-63289-0.00012-0.
[13] Sanchez-Sanchez A, Izquierdo MT, Mathieu S, González-Álvarez J, Celzard A, Fierro V. Outstanding electrochemical performance of highly N- and O-doped carbons derived from pine tannin. Green Chem 2017;19:2653–65. https://doi.org/10.1039/C7GC00491E.
[14] Sanchez-Sanchez A, Martinez de Yuso A, Braghiroli FL, Izquierdo MT, Alvarez ED, Pérez-Cappe E, et al. Sugarcane molasses as a pseudocapacitive material for supercapacitors. RSC Adv 2016;6:88826–36. https://doi.org/10.1039/C6RA16314A.
[15] Axelsson L, Franzén M, Ostwald M, Berndes G, Lakshmi G, Ravindranath NH. Jatropha cultivation in southern India: assessing farmers' experiences. Biofuels, Bioprod Biorefin 2012;6:246–56. https://doi.org/10.1002/bbb.1324.
[16] Hoekman SK, Broch A, Robbins C, Zielinska B, Felix L. Hydrothermal carbonization (HTC) of selected woody and herbaceous biomass feedstocks. Biomass Convers Biorefin 2013;3:113–26. https://doi.org/10.1007/s13399-012-0066-y.
[17] Tusi MM, Brandalise M, Verjúlio-Silva RWR, Correa OV, Villalba JC, Anaissi FJ, et al. Preparation of PtRu/C electrocatalysts by hydrothermal carbonization using different carbon sources Elsevier. Stud Surf Sci Catal 2010;175:551–4. https://doi.org/10.1016/S0167-2991(10)75106-5.
[18] Makowski P, Demir Cakan R, Antonietti M, Goettmann F, Titirici M-M. Selective partial hydrogenation of hydroxy aromatic derivatives with palladium nanoparticles supported on hydrophilic carbon. Chem Commun 2008;8:999–1001. https://doi.org/10.1039/b717928f.
[19] Qian H-S, Antonietti M, Yu S-H. Hybrid, "Golden Fleece": Synthesis and catalytic performance of uniform carbon nanofibers and silica nanotubes embedded with a high population of noble-metal nanoparticles. Adv Funct Mater 2007;17:637–43. https://doi.org/10.1002/adfm.200600657.
[20] Zhai D, Du H, Li B, Zhu Y, Kang F. Porous graphitic carbons prepared by combining chemical activation with catalytic graphitization. Carbon 2011;49:725–9. https://doi.org/10.1016/j.carbon.2010.09.057.
[21] Wang Z, Zhang X, Liu X, Lv M, Yang K, Meng J. Co-gelation synthesis of porous graphitic carbons with high surface area and their applications. Carbon 2011;49:161–9. https://doi.org/10.1016/j.carbon.2010.08.056.
[22] Fu R, Baumann TF, Cronin S, Dresselhaus G, Dresselhaus MS, Satcher JH. Formation of graphitic structures in cobalt- and nickel-doped carbon aerogels. Langmuir 2005;21:2647–51. https://doi.org/10.1021/la047344d.
[23] Dahn JR, Zheng T, Liu Y, Xue JS. Mechanisms for lithium insertion in carbonaceous materials. Science 1995;270:590–3. https://doi.org/10.1126/science.270.5236.590.
[24] Xie M, Yang J, Liang J, Guo X, Ding W. In situ hydrothermal deposition as an efficient catalyst supporting method towards low-temperature graphitization of amorphous carbon. Carbon 2014;77:215–25. https://doi.org/10.1016/j.carbon.2014.05.024.
[25] Neimark AV, Lin Y, Ravikovitch PI, Thommes M. Quenched solid density functional theory and pore size analysis of micro-mesoporous carbons. Carbon 2009;47:1617–28. https://doi.org/10.1016/j.carbon.2009.01.050.
[26] Scofield JH. Hartree-Slater subshell photoionization cross-sections at 1254 and 1487 eV. J Electron Spectrosc Relat Phenom 1976;8:129–37. https://doi.org/10.1016/0368-2048(76)80015-1.
[27] Thommes M, Kaneko K, Neimark AV, Olivier JP, Rodriguez-Reinoso F, Rouquerol J, et al. Physisorption of gases, with special reference to the evaluation of surface area and pore size distribution (IUPAC Technical Report). Pure Appl Chem 2015;87:1051–69. https://doi.org/10.1515/pac-2014-1117.
[28] Calderon B, Smith F, Aracil I, Fullana A. Green synthesis of thin shell carbon-encapsulated iron nanoparticles via hydrothermal varbonization. ACS Sustainable Chem Eng 2018;6:7995–8002. https://doi.org/10.1021/acssuschemeng.8b01416.
[29] Liu M, Gan L, Xiong W, Zhao F, Fan X, Zhu D, et al. Nickel-doped activated mesoporous carbon microspheres with partially graphitic structure for supercapacitors. Energy Fuels 2013;27:1168–73. https://doi.org/10.1021/ef302028j.
[30] Jana P, Palomo del Barrio E, Fierro V, Medjahdi G, Celzard A. Design of carbon foams for seasonal solar thermal energy storage. Carbon 2016;109:771–87. https://doi.org/10.1016/j.carbon.2016.08.048.
[31] Hussein TM, Nasir EM, Al-Aarajiy AH. Structural and surface morphology analysis of nickel phthalocyanine thin films. Adv Mater Phys Chem 2013;03:113–9. https://doi.org/10.4236/ampc.2013.31A014.
[32] Milev AS, Tran N, Kamali Kannangara GS, Wilson MA, Avramov I. Polymorphic transformation of iron-phthalocyanine and the effect on carbon nanotube synthesis. J Phys Chem C 2008;112:5339–47. https://doi.org/10.1021/jp710923f.
[33] Bilgin A, Ertem B, Gök Y. Highly organosoluble metal-free phthalocyanines and metallophthalocyanines: Synthesis and characterization. Eur J Inorg Chem 2007;2007:1703–12. https://doi.org/10.1002/ejic.200600943.
[34] Zhong C, He A, Guo R, Wu Q, Huang H. Synthesis, characterization and redox behavior of nickel(II) and cobalt(II) polymeric complexes. Synth Met 2008;158:33–7. https://doi.org/10.1016/j.synthmet.2007.11.007.
[35] Achar BN, Fohlen GM, Parkers JA, Keshavayya J. Synthesis and structural studies of metal 4,9,16,23-phthalocyanine tetraamines. Polyhedron 1987;6:1463–7. https://doi.org/10.1016/s0277-5387(00)80910-9.
[36] Shirai H, Kobuyashi K, Takemue Y, Hojo N. Functional metal-porphyrazine derivatives and their polymers, 2. Synthesis and properties of polyimides containing metal-phthalocyanines. Makromol Chem 1979;180:2073–84. https://doi.org/10.1002/macp.1979.021800902.
[37] Laskoski M, Steffen W, Morton JGM, Smith MD, Bunz UHF. Synthesis and explosive decomposition of organometallic dehydro[18]annulenes: An access to carbon nanostructures. J Am Chem Soc 2002;124:13814–8. https://doi.org/10.1021/ja026809o.

[38] Braghiroli F, Fierro V, Szczurek A, Gadonneix P, Ghanbaja J, Parmentier J, et al. Hydrothermal treatment of tannin: A route to porous metal oxides and metal/carbon hybrid materials. Inorganics 2017;5:7. https://doi.org/10.3390/inorganics5010007.
[39] Bernard S, Beyssac O, Benzerara K, Findling N, Tzvetkov G, Brown GE. XANES, Raman and XRD study of anthracene-based cokes and saccharose-based chars submitted to high-temperature pyrolysis. Carbon 2010;48:2506–16. https://doi.org/10.1016/j.carbon.2010.03.024.
[40] Cançado LG, Jorio A, Pimenta MA. Measuring the absolute Raman cross section of nanographites as a function of laser energy and crystallite size. Phys Rev B 2007;76. https://doi.org/10.1103/PhysRevB.76.064304.
[41] Lespade P, Marchand A, Couzi M, Cruege F. Caracterisation de materiaux carbones par microspectrometrie Raman. Carbon 1984;22:375–85. https://doi.org/10.1016/0008-6223(84)90009-5.
[42] Ferrari AC. Raman spectroscopy of graphene and graphite: Disorder, electron–phonon coupling, doping and nonadiabatic effects. Solid State Commun 2007;143:47–57. https://doi.org/10.1016/j.ssc.2007.03.052.
[43] Maldonado-Hódar FJ, Moreno-Castilla C, Rivera-Utrilla J, Hanzawa Y, Yamada Y. Catalytic graphitization of carbon aerogels by transition metals. Langmuir 2000;16:4367–73. https://doi.org/10.1021/la991080r.
[44] Beams R, Gustavo Cançado L, Novotny L. Raman characterization of defects and dopants in graphene 083002. J Phys: Condens Matter 2015;27. https://doi.org/10.1088/0953-8984/27/8/083002.
[45] Shen W, Fan W. Nitrogen-containing porous carbons: synthesis and application. J Mater Chem A 2013;1:999–1013. https://doi.org/10.1039/C2TA00028H.
[46] Vallejos-Burgos F, Utsumi S, Hattori Y, García X, Gordon AL, Kanoh H, et al. Pyrolyzed phthalocyanines as surrogate carbon catalysts: Initial insights into oxygen-transfer mechanisms. Fuel 2012;99:106–17. https://doi.org/10.1016/j.fuel.2012.03.055.
[47] Carley AF, Jackson SD, O'Shea JN, Roberts MW. The formation and characterisation of Ni3+ — an X-ray photoelectron spectroscopic investigation of potassium-doped Ni(110)–O. Surf Sci 1999;440:L868–74. https://doi.org/10.1016/S0039-6028(99)00872-9.
[48] Gupta RP, Sen SK. Calculation of multiplet structure of core p -vacancy levels. II. Phys Rev B 1975;12:15–9. https://doi.org/10.1103/PhysRevB.12.15.
[49] Brundle CR, Chuang TJ, Wandelt K. Core and valence level photoemission studies of iron oxide surfaces and the oxidation of iron. Surf Sci 1977;68:459–68. https://doi.org/10.1016/0039-6028(77)90239-4.
[50] Biesinger MC, Payne BP, Lau LWM, Gerson A, Smart RStC. X-ray photoelectron spectroscopic chemical state quantification of mixed nickel metal, oxide and hydroxide systems. Surf Interface Anal 2009;41:324–32. https://doi.org/10.1002/sia.3026.
[51] Figueiredo JL, Pereira MFR. The role of surface chemistry in catalysis with carbons. Catal Today 2010;150:2–7. https://doi.org/10.1016/j.cattod.2009.04.010.
[52] Liu X, Osaka T. Properties of electric double-layer capacitors with various polymer gel electrolytes. J Electrochem Soc 1997;144:3066–71. https://doi.org/10.1149/1.1837960.
[53] Inagaki M, Konno H, Tanaike O. Carbon materials for electrochemical capacitors. J Power Sources 2010;195:7880–903. https://doi.org/10.1016/j.jpowsour.2010.06.036.
[54] Li H, Guo H, Huang K, Liu B, Zhang C, Chen X, et al. Carbon electrode with conductivity improvement using silver nanowires for high-performance supercapacitor. Appl Phys A 2018;124:763. https://doi.org/10.1007/s00339-018-2182-4.
[55] Fujii H. Effects of the electron-withdrawing power of substituents on the electronic structure and reactivity in oxoiron(IV) porphyrin π-cation radical complexes. J Am Chem Soc 1993;115:4641–8. https://doi.org/10.1021/ja00064a027.
[56] Barton SS, Koresh JE. A study of the surface oxides on carbon cloth by electrical conductivity. Carbon 1984;22:481–5. https://doi.org/10.1016/0008-6223(84)90079-4.
[57] Oh YJ, Yoo JJ, Kim YI, Yoon JK, Yoon HN, Kim J-H, et al. Oxygen functional groups and electrochemical capacitive behavior of incompletely reduced graphene oxides as a thin-film electrode of supercapacitor. Electrochim Acta 2014;116:118–28. https://doi.org/10.1016/j.electacta.2013.11.040.
[58] Byon HR, Gallant BM, Lee SW, Shao-Horn Y. Role of oxygen functional groups in carbon nanotube/graphene freestanding electrodes for high performance lithium batteries. Adv Funct Mater 2013;23:1037–45. https://doi.org/10.1002/adfm.201200697.
[59] Pantea D, Darmstadt H, Kaliaguine S, Roy C. Electrical conductivity of conductive carbon blacks: Influence of surface chemistry and topology. Appl Surf Sci 2003;217:181–93. https://doi.org/10.1016/S0169-4332(03)00550-6.
[60] Li Gangyong, Li Zihan, Xiao Xiang, An Yuanlin, Wang Wei (Alex), Hu Zongqian. An ultrahigh electron-donating quaternary-N-doped reduced graphene oxide@carbon nanotube framework: a covalently coupled catalyst support for enzymatic bioelectrodes. J Mater Chem A 2019;7(18):11077–85. https://doi.org/10.1039/C9TA00771G.
[61] Xu Z, Li Z, Holt CMB, Tan X, Wang H, Amirkhiz BS, et al. Electrochemical supercapacitor electrodes from sponge-like graphene nanoarchitectures with ultrahigh power density. J Phys Chem Lett 2012;3:2928–33. https://doi.org/10.1021/jz301207g.
[62] Liu T, Liu E, Ding R, Luo Z, Hu T, Li Z. Preparation and supercapacitive performance of clew-like porous nanocarbons derived from sucrose by catalytic graphitization. Electrochim Acta 2015;173:50–8. https://doi.org/10.1016/j.electacta.2015.05.042.
[63] Gutiérrez-Pardo A, Ramírez-Rico J, Cabezas-Rodríguez R, Martínez-Fernández J. Effect of catalytic graphitization on the electrochemical behavior of wood derived carbons for use in supercapacitors. J Power Sources 2015;278:18–26. https://doi.org/10.1016/j.jpowsour.2014.12.030.
[64] Zhu Y, Hu H, Li W-C, Zhang X. Cresol–formaldehyde based carbon aerogel as electrode material for electrochemical capacitor. J Power Sources 2006;162:738–42. https://doi.org/10.1016/j.jpowsour.2006.06.049.
[65] Liu Y, Liu Q, Gu J, Kang D, Zhou F, Zhang W, et al. Highly porous graphitic materials prepared by catalytic graphitization. Carbon 2013;64:132–40. https://doi.org/10.1016/j.carbon.2013.07.044.